RSC Advances

PAPER

View Article Online
View Journal | View Issue

Cite this: *RSC Adv.*, 2023, **13**, 24162

From waste to energy storage: calcinating and carbonizing chicken eggshells into electrode materials for supercapacitors and lithium-ion batteries†

Agnieszka Gabryelczyk, *[a] Sudesh Yadav, [b] Agnieszka Swiderska-Mocek,[a] Ali Altaee[b] and Grzegorz Lota *[ac]

The presented study aims to explore the potential sources of common bio-wastes that could be successfully processed without any leftovers into materials for energy conversion and storage devices. We used chicken eggshells as an environmentally friendly precursor for electrode fillers in electrochemical capacitors (calcinated OS_{600} and OS_{900}) and anode materials in Li-ion batteries (carbonized EM_{600} and EM_{900}). Both groups of materials were obtained at two different temperatures to investigate the influence of their composition and properties on the electrochemical performance. Electrochemical capacitors with OS_{600} and OS_{900} substituted for 10 wt% of commercial activated carbon supplied similar capacitances, with OS_{600} stabilizing the long-term performance of the device. Also, both obtained anode materials are suitable for operation in Li-ion batteries, supplying a capacity of around 280 mA h g^{-1}. Notably, EM_{900} is characterized by a well-developed structure, and as an anode, it exhibited better capacity retention of over 84%.

Received 7th May 2023
Accepted 7th August 2023

DOI: 10.1039/d3ra03037g

rsc.li/rsc-advances

Introduction

Sustainability aims to preserve equal and uninterrupted access to all resources for the present and future generations. This task is not trivial due to the growing demand for food, drinking water, manufactured goods, services, and energy. Energy conversion is one of the main concerns of sustainability since it prevails in technological and scientific development, manufacturing, and daily life. However, most of the energy demand is satisfied by the combustion of fossil fuels, which creates pressure on the natural environment through mining and the generation of harmful gaseous products such as NO_x and SO_x. Reducing fossil fuel consumption for energy generation has become the focus of modern innovations. A visible result of these actions is a growing number of solar cells for both grid power and individual and the various wind and water-based power plants. Solar radiation, blowing wind, and masses of water accumulate a large amount of energy that can be accessed and converted into electricity without producing harmful byproducts. However, these environmentally friendly energy sources are limited by their periodic availability. Supporting renewable energy sources and power plants by storing surplus energy can overcome this issue.

Many devices enable efficient storage and immediate recovery of accumulated energy through electricity. The most important ones are electrochemical capacitors and batteries. These two groups store energy following different working mechanisms. Batteries (*e.g.*, lithium-ion batteries LIBs, lead–acid batteries LABs, nickel–metal hydride batteries, NiMH) alternately convert chemical energy to electricity based on various redox reactions. On the other hand, conventional electrochemical capacitors (ECs), also known as supercapacitors, usually store charged species electrostatically, forming a double layer at the electrode/electrolyte interface.[1] Regardless of the working principle, both groups of devices display complementary properties and functions. Generally, batteries exhibit a higher energy density, so they are more suitable for long-term off-grid energy storage and charging/discharging at a moderate rate for a longer time.[1,2] On the other hand, electrochemical capacitors (ECs) show high power density and power capability, while their energy density is usually lower.[1,3] These characteristics of electrochemical capacitors make them suitable for rapid charging/discharging under demand for high current, as in regenerative braking and supporting battery packs in electric vehicles.[1,4]

[a]*Faculty of Chemical Technology, Institute of Chemistry and Technical Electrochemistry, Poznan University of Technology, Berdychowo 4, 60-965 Poznan, Poland. E-mail: grzegorz.lota@put.poznan.pl; agnieszka.gabryelczyk@put.poznan.pl*

[b]*Centre for Green Technology, School of Civil and Environmental Engineering, University of Technology Sydney, 15 Broadway, NSW, 2007, Australia*

[c]*Łukasiewicz Research Network – Institute of Non-Ferrous Metals Division in Poznan, Central Laboratory of Batteries and Cells, Forteczna 12, 61-362 Poznan, Poland*

† Electronic supplementary information (ESI) available. See DOI: https://doi.org/10.1039/d3ra03037g

In electrochemical power sources, the electrodes facilitate the transfer of electrons. They can store the charge physically by electrostatic force (EC) or chemically react with charge carriers and change their chemical composition to convert energy (batteries). Some capacitors (*e.g.*, pseudocapacitors and hybrid capacitors) rely on both mechanisms, coupling electrostatic charge storage with faradaic reactions. Electrode materials are indispensable and belong to the most expensive components in electrochemical power sources. Reducing its cost lowers the price of the whole battery or electrochemical capacitor. Electrochemical capacitors and lithium-ion batteries (LIBs) rely on carbon derivatives as some of their electrodes of choice. Activated carbon commonly serves as a negative and positive electrode in EC, while graphite is an anode material in LIBs. The relatively cheap precursor of these electrode materials comes from carbon-rich organic wastes. To date, it has been successfully produced from various plant fibres,[5–7] litchi shells,[8] spent coffee beans,[9] and many more.

Recent studies show that a new widely accessible, inexpensive, and non-toxic source of carbon can be chicken eggshells (EGS).[10–15] EG consists of an outer layer of eggshell (OS) and an eggshell membrane (EM). The outer mineral layer comprises calcium carbonate, while the inner layer comprises carbon and heteroatom-rich proteins[15] (Fig. 1). Both layers can be efficiently processed and reused: OS by high-temperature calcination producing calcium oxide[14] (i), EM by carbonization and subsequent activation[16] (ii). Products of these reactions are suitable for application in energy conversion and storage,[12,14] membrane purification techniques,[17] or even catalysis.[18,19] Furthermore, even a non-processed EM is promising for multiple applications. Cleaned EM was used in a biocompatible piezoelectric nanogenerator,[13] which could potentially work in small devices measuring heart rate or joint movements. Furthermore, the thinness and the porous free-standing structure of EM make it a potential separator for Li-ion batteries[20,21] and supercapacitors based on neutral aqueous electrolytes.[22] Calcinated EGS has been used as active anode material in the Li-ion capacitor.[12] Furthermore, carbonized EM has served as an active material for electrodes in supercapacitors[10] and anodes in both Li–S[16] and Li-ion batteries.[11]

The presented study exploits chicken eggshell-derived products as cheap bio-derived components for electrochemical capacitors and Li-ion batteries. The eggshell layers have been separated and applied in different energy storage devices to create tailored electrodes for each of them, with optimal composition and properties rivalling those of the commercial materials. The aim of such approach is to maximize the utilization of this waste material. The outer layer (OS) has been calcinated and used as a scaffold to increase the efficacy of activated carbon in electrodes for symmetric electrochemical capacitors, which is a novelty in the area of eggshell-based materials. This way, less activated carbon is required to achieve similar performance of an electrochemical capacitor. The carbonized inner layer (EM) has been used as the anode material in Li-ion batteries as a cheaper alternative to graphite. The study aims to explain the production technology of electrode materials from common bio-wastes and compare the physicochemical properties and applicability of the materials obtained under different thermal conditions. Furthermore, discussed results highlight the benefits of using bio-wastes as sustainable precursors of electrode materials for energy conversion and storage.

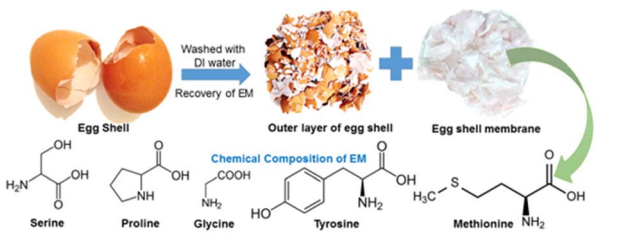

Fig. 1 Separation of calcite-rich outer eggshell and inner membrane from the raw eggshell and the chemical composition of EM.

Results and discussion

Physicochemical characterization

Thermogravimetric analysis (Fig. 2) of the obtained calcinated and carbonized materials consists of thermogravimetric curves (TGA) and derivative thermogravimetric curves (DTG). The measurement aimed to test the stability of the obtained electrode materials.

Calcinated outer eggshells OS_{600} (Fig. 2a) and OS_{900} (Fig. 2b) undergo two decomposition stages. Both materials experience the first decomposition step at around 380–450 °C. It is attributed to the dehydration of calcium hydroxide $Ca(OH)_2$. Generally, calcium oxide CaO readily absorbs moisture from the air to form $Ca(OH)_2$, which decomposes above 350 °C.[23] The measured mass loss is significantly higher for OS_{900} (mass loss of 25 wt%), which consists almost purely of CaO. The second step for OS_{600} occurs above 730 °C when calcium carbonate $CaCO_3$ calcinates to CaO generating CO_2.[2] OS_{900} displays only a minor second decomposition step at 600 °C, responsible for only 1 wt% loss of the sample.

Carbonized EM_{600} (Fig. 2c) and EM_{900} (Fig. 2d) also undergo two visible thermal changes in the nitrogen atmosphere. In the case of EM_{600}, the first process occurs between 70–120 °C and can be attributed to the evaporation of water and highly volatile matter. The second step begins above 640 °C and consumes approx. 10 wt% of the material indicates further carbonization of the remaining organic matter. EM_{900} undergoes the evaporation of water and volatile species around 50–90 °C, followed by a weak mass loss (around 2 wt%) around 470 °C, which could be related to a degradation of the remaining volatile matter. In both cases, there is a high amount of solid carbon-rich residue of 82 wt% for EM_{600} and 88 wt% for EM_{900}. The mass loss of EM_{900} is lower than that of EM_{600} due to the production conditions of the material. Namely, EM_{900} reached a higher degree of carbonization during pyrolysis at 900 °C, when the organic substrate was subjected to dehydrogenation (i) and condensation of aromatic structure (ii), whose C–C bonds possess high energy and hence, are stable.[24] Since processes (i) and (ii) proceed mostly above 600 °C, EM_{600} has a less

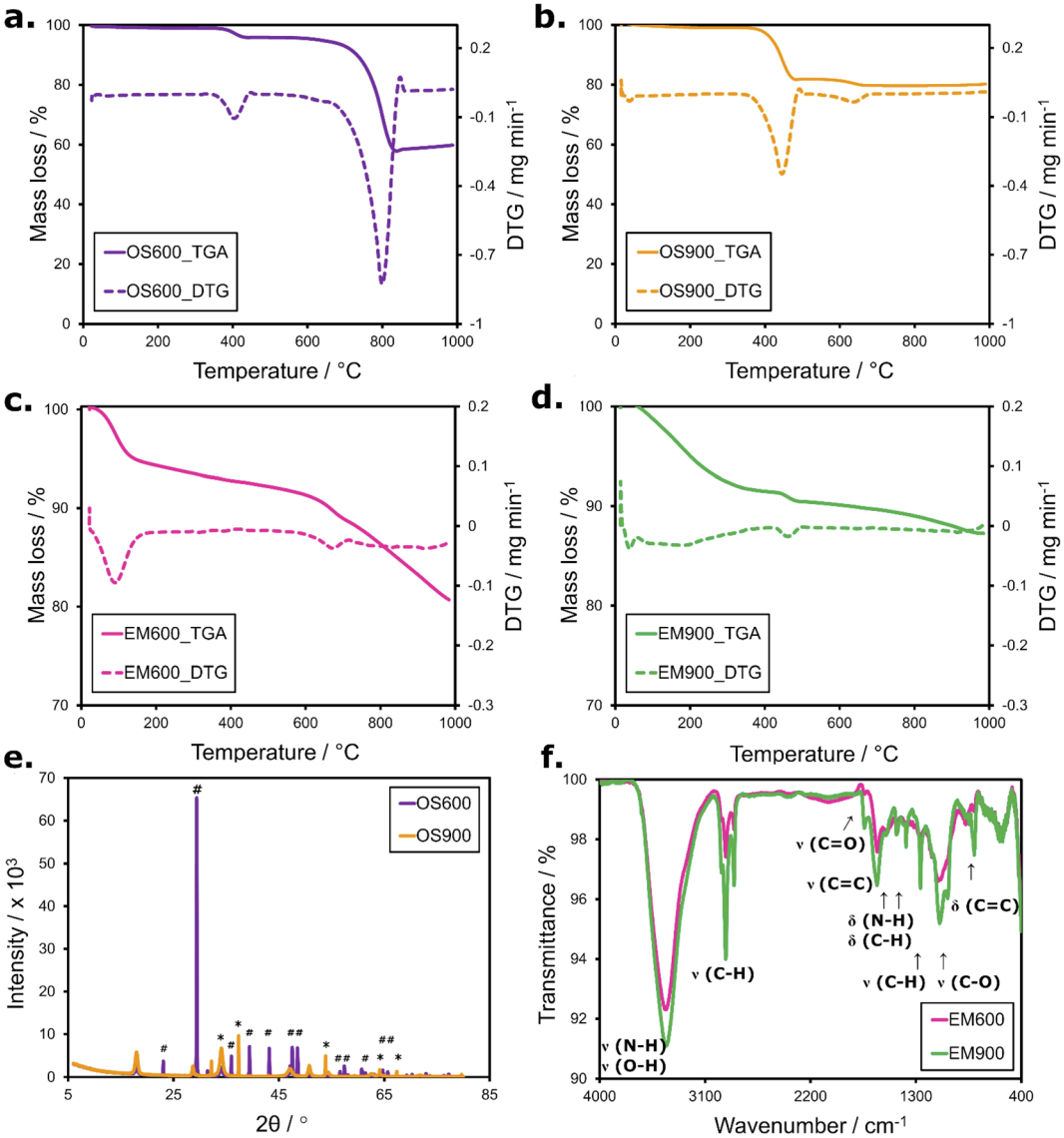

Fig. 2 TGA and DTG curves of calcinated outer eggshells (a and b) and the carbonized inner eggshell membranes (c and d). X-ray diffractogram of calcinated outer eggshells OS_{600} and OS_{900} (e). FTIR spectra of carbonized eggshell membranes (f).

condensed chemical structure, with characterized by aryl compounds losing their side chains.[24] The overall residual mass of EM_{600} and EM_{900} at 1000 °C is high because it cannot combust in the nitrogen atmosphere. Over 80 wt% of solid residue indicates a high degree of carbonization and acceptable content of volatile organic matter in the obtained electrode materials.

The X-ray diffractogram (Fig. 2e) of OS_{600} confirms that this material consists primarily of polymorph calcite $CaCO_3$, as the pattern obtained pattern matches the standard.[14] Calcite crystals (label # on the diffractogram) grow typically for the compound, clearly favouring the plane (104) at the 2θ = 29.5°.[12,14] The peaks are evident but much weaker, indicating the preferred orientation of the calcite crystals. All peaks are narrow, suggesting a regular well-developed crystalline structure. Calcinating the outer chicken eggshell at 900 °C changed the crystal structure and composition of OS_{900}. $CaCO_3$ was mostly converted to calcium oxide CaO (label * on the diffractogram). There is only a weak peak at 29.4° which suggests the presence of the remaining calcite phase. Very weak peaks at 34.2, 47.2, and 50.8° could be attributed to the formation of the $Ca(OH)_2$ phase from CaO due to exposure to moisture from the air.[25] The TGA data also support the presence of such a phase.

With the FT-IR spectra (Fig. 2f), we identified the characteristic bonds within the carbonized eggshell membrane EM_{600} and EM_{900}. Both materials interact similarly with a light beam, resulting in almost overlapping spectra, which indicates their similar chemical structure. The bonding involves carbon, hydrogen, nitrogen, and oxygen. Strong and broad peaks at 3600–3100 cm^{-1} correspond to the stretching vibration of N–H and O–H bonds. Then follow medium, narrow signals from stretching vibrations of alkyl C–H bonds. Medium-intensity

Table 1 The average elemental composition of EM_{600} and EM_{900}

Sample	C (%)	N (%)	H (%)
EM_{600}	73.73	11.75	2.02
EM_{900}	81.30	6.77	1.67

bands at 1628, 1555, and ~810 cm^{-1} are related to the aryl C=C stretching mode. Carbon is also identified in other bonds: ketone group C=O at 1738 cm^{-1} and alkyl C–H bond at 1460/1384 cm^{-1} (bending mode and stretching mode, respectively). Ma *et al.*[15] and Xie *et al.*[26] reported the presence of these bonds, similarly located in their material derived from the eggshell membrane. As the transmittance of EM_{900} is slightly lower than that of EM_{600} at all wavelengths, EM_{900} contains higher populations of bonds that absorb the incident light. Presumably, the reason lies in the higher carbonization of that bio-waste material.

Elemental analysis (Table 1) determined that the main components of the carbonized inner eggshell membranes EM_{600} and EM_{900} are carbon, nitrogen, and hydrogen. This result agrees with the FT-IR data, which detected the presence of functional groups and bonds involving these three elements. The carbon content significantly increases from 73.7 wt% to 81.3 wt% with the pyrolysis temperature because the high-temperature process ensures that organic wastes reach a higher degree of carbonization. However, there was no detectable sulfur or phosphorus in either sample despite the S- and P-rich proteins building the eggshell membranes. Likely, these elements evaporated during the carbonization of eggshell membranes, *e.g.*, hydrogen sulfide H_2S, released upon heating proteins above 350 °C.[27]

Electrochemical performance

Electrochemical capacitors. The outer eggshells calcinated at two different temperatures consist mainly of calcium compounds, but their exact composition varies depending on the calcination temperature. OS_{600} contains predominantly calcium carbonate, while OS_{900} contains calcium oxide with a small addition of calcium hydroxide. Because of such a composition, these materials do not meet a standard of sufficient conductivity for use in chemical power sources. However, they could still be beneficial as an inert, ceramic scaffold which allows for better distribution of the carbon-based active material, thus, reducing its content without aggravating the operating parameters of ECs. To validate this possibility, calcinated materials OS_{600} and OS_{900} were mixed with a commercial activated carbon YP-80F in a gravimetric ratio of

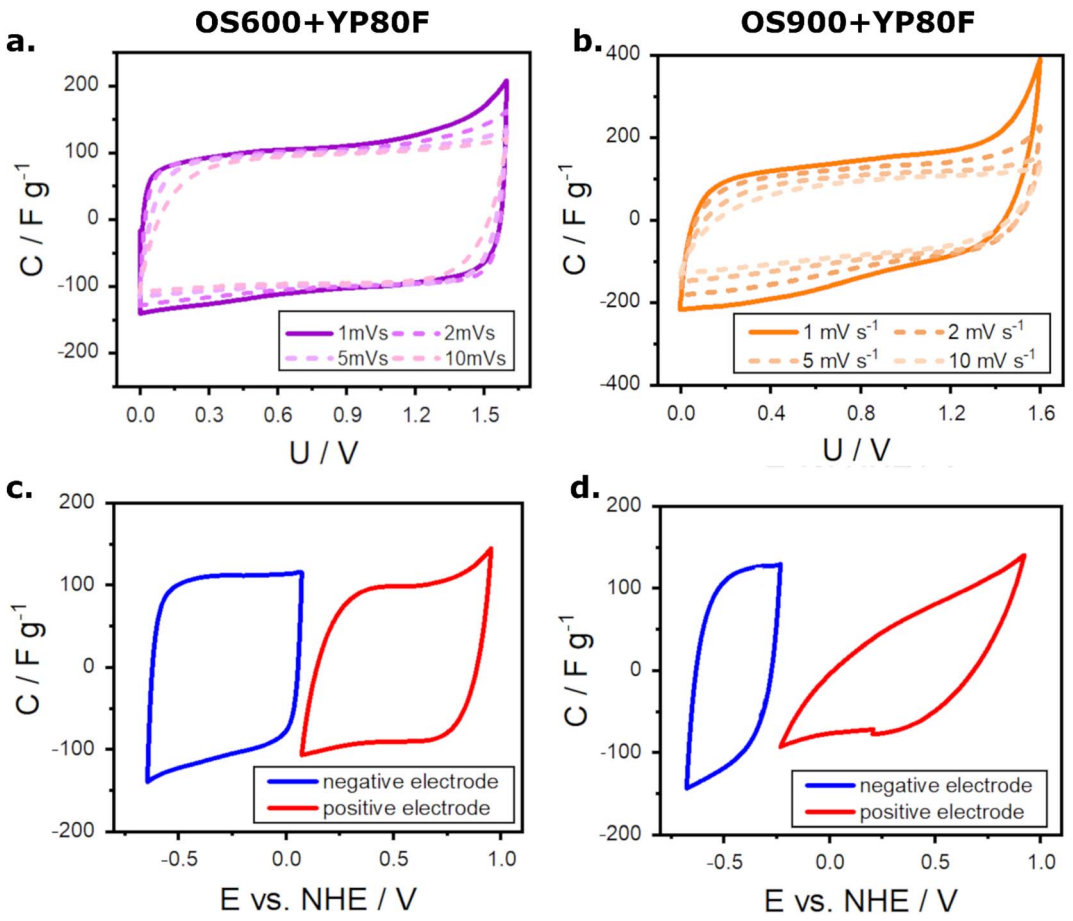

Fig. 3 Cyclic voltammetry performed at different scan rates (two-electrode cell) of hybrid material OS_{600}+YP80F (a) and OS_{900}+YP80F (b), cyclic voltammetry performed at 5 mV s^{-1} (three-electrode cell) of hybrid material OS_{600}+YP80F (c) and OS_{900}+YP80F (d).

1 : 9. The tested ECs were labelled OS_{600}+YP80F and OS_{900}+YP80F, respectively. The calculated performance of ECs is summarized in Table S1 of the ESI.†

The first test performed on ECs assessed the capacitance at different CV scan rates (Fig. 3a and b). At a lower scan rate, both supercapacitors exhibit typical capacitance for symmetric ECs with electrodes made of YP-80F in an aqueous electrolyte of 1 M Na_2SO_4, which falls around 109–125 F g^{-1}.[28,29] Comparison of the Fig. 3a and b show that the substitution of 10 wt% of YP-80F with OS_{600} improves the long-term term and high-scan rate specific capacitance of the ECs, compared to the substitution with OS_{900}. Likely, it is a result of a higher conductivity of $CaCO_3$ (OS_{600}) than CaO (OS_{900}). Although the initial capacitance of OS_{900}+YP80F at 1 and 2 mV s^{-1} is higher than that of OS_{600}+YP80F (131.4 and 111.7 F g^{-1} *vs.* 107.6 and 101.5 F g^{-1}), the tendency changes to the opposite one at higher rates. The capacitance of OS_{600}+YP80F at a scan rate of 5 mV s^{-1} equals 94 F g^{-1} while that of OS_{900}+YP80F to 91 F g^{-1}. This discrepancy grows with the increasing scan rate. The values finally drop to 47 and 27 F g^{-1} at a scan rate of 100 mV s^{-1}, respectively. Moreover, modification with OS_{600} results in a regular, rectangular shape of CV curves, while OS_{900} accelerates oxygen evolution above the voltage of 1.3 V. The test showed that the modification with OS_{600} prevents fast degeneration of the material, reduces the internal resistance, and maintains acceptable capacitance retention at moderate scan rates.

Three-electrode measurements (Fig. 3c and d) indicate that modification of electrode material with OS_{600} allows for keeping low internal resistance of the electrodes, which can be ascribed to the well-shaped rectangular voltammograms. On the other hand, the presence of OS_{900} caused a sharp increase in the internal resistance, which is indicated by the shape of the voltammograms. The other visible effect is a shift in the working potential. The negative electrode in the OS_{900}+YP80F supercapacitor works in a narrower area. These observations are related to reduced capacitances of the negative and positive electrodes.

Fig. 4a presents the impedance spectra of both ECs in the form of Nyquist plots. Both plots have a similar shape and consist of two main areas. At high frequencies, there is a half-circle, followed by a short steep slope related to the diffusion of ions in a porous material and a long, nearly vertical line at low frequencies related to the capacitive performance of the ECs. Such plots are typically encountered in the case of ECs.[30–32] The most accurate fitting of the impedance spectra was obtained for an equivalent electrical circuit depicted in Fig. 4b. It consists of an element R_1, ascribed to the electrolyte and separator resistance (ohmic resistance). The next element, C_{dl}, refers to the capacitance of the double layer, which forms on the electrolyte/electrode interface. R_{ct} is attributed to the charge transfer resistance through that interface. An element W, the so-called Warburg impedance, is in the intermediary frequencies. It indicates that the process occurring in this area is hindered diffusion through a porous material. However, low values of element W suggest that the resistance of this element is not significantly disturbing the operation of EC. At low frequencies, the diffusion element transits to C_1, which is responsible for the capacitive behaviour of the device. The fitting procedure revealed that OS_{600}+YP80F exhibits lower ohmic and charge transfer resistances than OS_{900}+YP80F (0.399 and 36.2 Ω, respectively, for OS_{600}−YP80F; 0.463 and 53.3 Ω for OS_{900}+YP80F). Presumably, the lower resistance of OS_{600}+YP80F result from better wetting of a carbon material modified by hydrophilic calcium carbonate and ionic conductivity of this salt, which is higher than that of calcium oxide. However, the capacitive behavior of the material reflected by C_1 is more prominent for OS_{900}+YP80F with 0.355 F, while it equals 0.269 F for OS_{600}+YP80F. This result could be justified by stronger electrostatic interactions found in calcium oxide, the component of OS_{900}.

A performance test followed the above-described measurements. It comprised cycling under a load of 1 A g^{-1} (Fig. 5a), self-discharge of the ECs over the time of 20 h (Fig. 5b), and the comparison of cyclic voltammetry at a scan rate of 10 mV s^{-1} before and after 5000 cycles at 1 A g^{-1} (Fig. 5c and d). The cyclic performance of OS_{600}+YP80F is uniform throughout the 5000 cycles, with a high retention of capacitance reaching 87% (initial capacitance ~ 108 F g^{-1}; the final one ~ 94 F g^{-1}). The

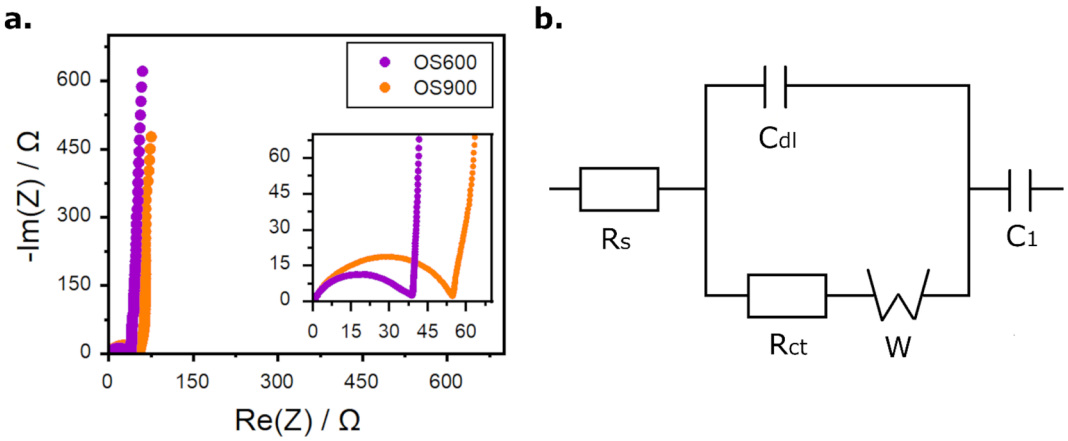

Fig. 4 Nyquist plots before cycling for ECs working in 1 M Na_2SO_4 with electrode material consisting of OS_{600}+YP80F and OS_{900}+YP80F (a). Equivalent circuit fitted to the Nyquist plots of both ECs (b).

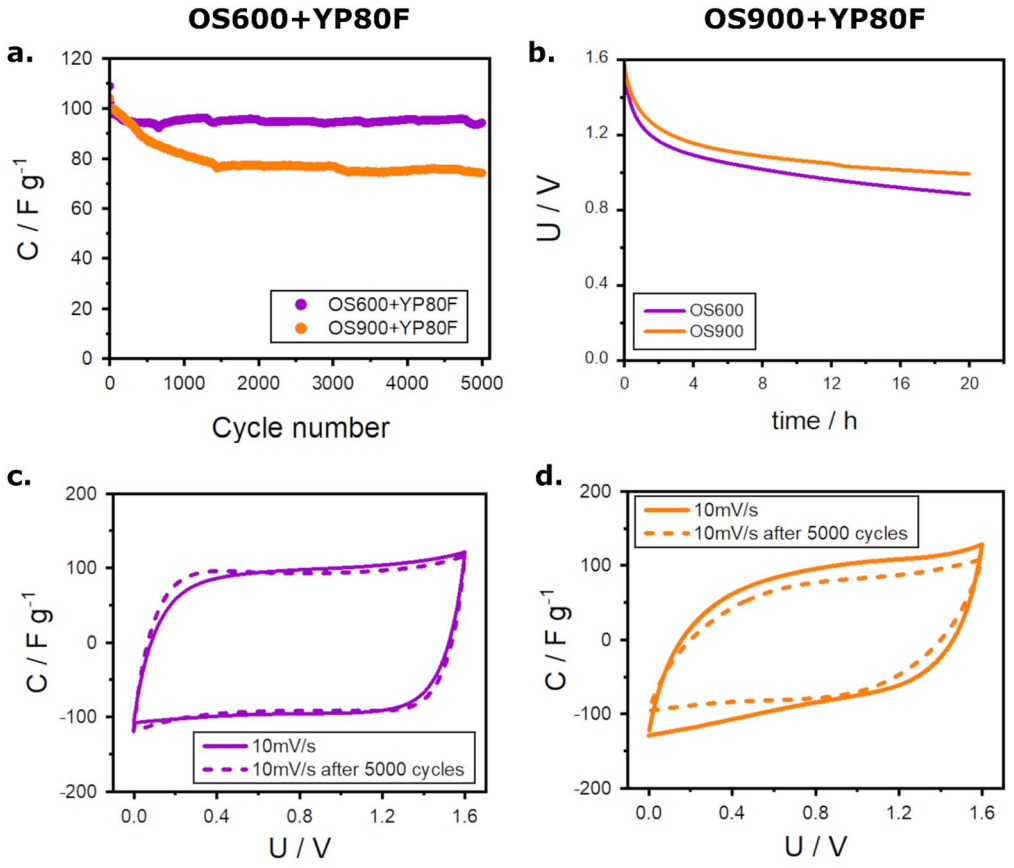

Fig. 5 Cyclic performance of ECs at the current load of 1 A g^{-1} (a), self-discharge (b), cyclic voltammetry before and after cycling of ECs with OS_{600}+YP80F material (c) and OS_{900}+YP80F material (d), all in two-electrode cell.

undesired capacitance fading upon cycling is greater in the case of OS_{900}+YP80F. The capacitance of this EC decreases gradually during the first 1500 cycles until the loss reaches 29% (from ~104 to ~75 F g^{-1}). Still, it stabilizes afterwards, and this value remains similar for the remaining cycles. The operational stability of the electrochemical capacitors was estimated based on their self-discharge (Fig. 5b). The self-discharge is slightly slower in the presence of OS_{900} in the electrode material. The values measured for OS_{900}+YP80F dropped from the initial 1.60 V to 1.33 V after 1 h, 1.13 V after 5 h, and 0.99 V after 20 h. In the same time intervals, the self-discharge of the OS_{600}+YP80F capacitor was 1.25 V, 1.07 V, and 0.89 V, respectively. This parameter depends strongly on charge redistribution.[33] It is affected by pores size, shape, and distribution and by the adsorption properties of the electrode material.[34] Finely powdered OS_{900} could adjust the pore size of activated carbon and improve the adsorption of the charged species. Furthermore, OS_{900} composed of CaO is strongly electrostatic, which could improve self-discharge of the EC. Lastly, the final test was to evaluate the integrity of the electrodes after the performance test and the capacitance retention. The cyclic voltammograms show that substituting activated carbon with OS_{600} (Fig. 5c) prevents performance loss and resistance growth while cycling. Moreover, the CV curve of this EC retains its proper rectangular shape after cycling and almost overlaps with the previous one. On the other hand, modification with OS_{900} (Fig. 5d) is less beneficial for extensively cycled electrochemical capacitors. It causes a significant ohmic drop, and the capacity loss exceeds 20%.

Table 2 presents the estimated values of the contact angle of aqueous electrolytes on electrodes made of YP80F, OS_{600}+YP80F, and OS_{900}+YP80F. Due to the large content of the commercial activated carbon, binder, and carbon black, all contact angles are similar. Only the presence of OS_{600} in the electrode material slightly decreased the contact angle of the EC electrolyte on the electrode surface. Since calcite, which constitutes the main component of OS_{600}, is strongly hydrophilic, a drop of water on the surface of the pressed calcite pellets produces low contact angles.[35,36] Presumably, a slightly better wettability of OS_{600}+YP80F could be ascribed to the hydrophilic properties of calcite. As the capacitance of OS_{600}+YP80F becomes higher than that of OS_{900}+YP80F at faster

Table 2 The average values of the contact angle of 1 M Na_2SO_4 on the EC electrodes made of calcinated outer eggshell and modified hybrid materials

Sample	YP80F	OS_{600}+YP80F	OS_{900}+YP80F
Contact angle [°]	82 ± 2	79 ± 2	81 ± 2

scan rates (CV), and at higher loads (GCPL), it could be explained as a result of improved wetting of the porous material (Table S1†).

Lithium-ion batteries. Carbonization of inner eggshell membranes created two new active materials to be utilized as negative electrodes of lithium-ion batteries. Several techniques characterized the electrochemical properties of both materials. First, CV supplied information on the intercalation profiles of lithium ions in these materials and other reactions. Voltammograms of each anode material (Fig. 7) display three consecutive cycles that reflect the charging and discharging of the active material. Li^+ is transported to the carbon-based electrode and intercalated in this material during charging. This process is called intercalation. The reverse process occurs during discharging when the Li^+ is extracted from the carbon anode (deintercalation) and transported to the cathode.

Fig. 6a illustrates voltammograms of the EM_{600}-based electrode. The first charging causes a sharp decrease in the cathodic current (to -100 mA g^{-1}). A small peak at around 0.73 V *vs.* Li/Li^+ is attributed to the solid electrolyte interphase (SEI) formation. The SEI growth is irreversible and leads to the initial consumption of Li^+ and some electrolytes. The SEI formation results in a significant irreversible capacity after the first cycle. Afterwards, the cathodic current decreases steadily until the lower potential limit is approached. Comparing the three following cycles reveals that the intercalation process is not fully reversible. Li^+ intercalates the bio-derived carbon material during the first cycle, although the lack of distinct intercalation peaks suggests the process is hindered. The latter two cycles do not overlap with the first one, and the low currents indicate a slow kinetics of undergoing processes. A half-cell with EM_{600} displays a high irreversible capacity resulting from Li^+ not being fully removed from the material. It is probably caused by the poorly developed structure of the material without condensed aromatic rings and a moderate degree of carbonization, which were noticed based on the physicochemical analysis of the material. The other material, EM_{900}, is characterized by significantly better stability (Fig. 6b). The current fading after the first cycle is small, indicating quite low irreversible capacity. In the first cycle, a signal indicates the formation of the SEI (a small peak around 0.70 V *vs.* Li/Li^+). Consecutive cycles do not repeat such behaviour, meaning that SEI formation progresses appropriately during the initial phases of the battery operation and consumes only a relatively small fraction of Li^+. The peaks attributed to the intercalation process are observed during charging (cathodic process) below 0.30 V *vs.* Li/Li^+, which is typical for carbon-based materials.[37] Several peaks at low potentials (around 0.30 V, 0.22, and 0.08 V *vs.* Li/Li^+) suggest a well-developed intercalation progressing in stages. The intercalation process is reversible, which justifies a peak around 0.25 V *vs.* Li/Li^+. Similar behaviour repeats over the second and third cycles.

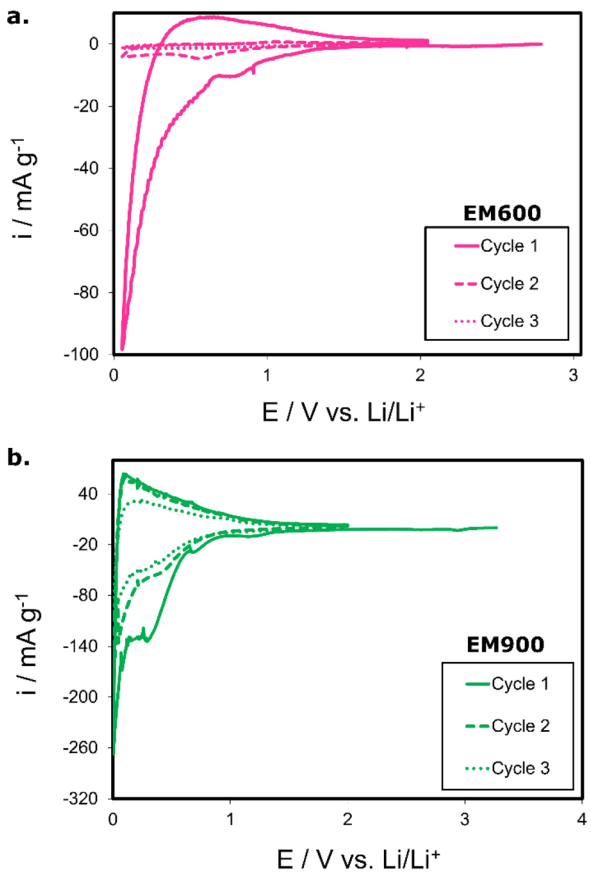

Fig. 6 Cyclic voltammograms of EM_{600} (a) and EM_{900}-based anode materials (b) were carried out in a 3-electrode configuration at the scan rate of 0.01 mV s^{-1}, between 2.0 and 0.01 V *vs.* Li/Li^+. Each voltammogram displays three consecutive cycles.

Moreover, the difference between the voltammetric curves of the second and third cycles is negligible. This electrochemical behaviour describes well-developed active material where Li^+ transport undergoes in both directions without unacceptable charge loss. Compared with EM_{600}, EM_{900} exhibits better stability over cycling with a smaller irreversible capacity after the first cycle and lower current response fading. All listed phenomena warrant reversible intercalation, and thus, they should account for a more stable long-cycling performance. The better intercalation characteristics are related to a higher degree of carbonization and condensation of EM_{900} resulting from a higher temperature of bio-wastes pyrolysis.

Fig. 7 presents the Nyquist plots of EM_{600} and EM_{900} half-cells. The measurement was performed twice for each anode material: on a freshly assembled cell and directly after the first charging. The spectra of anode materials EM_{600} (Fig. 7a) and EM_{900} (Fig. 7b) strongly resemble each other in both states. After assembly, the Nyquist spectra consist of a small semi-circle related to the charge transfer process and a long inclined line attributed to the anode's diffusion process and capacitive behaviour. The overall impedance is higher for a freshly assembled EM_{900} cell. After the EM_{600} and EM_{900} half-cells are charged, the resistances of the first semi-circles grow significantly, although the overall cell resistance drops sharply. In the charged (intercalated) state, there is only a slight difference between the shape of the impedance spectra of both cells. The first semi-circle has a similar impedance for both EM_{600} and EM_{900}.

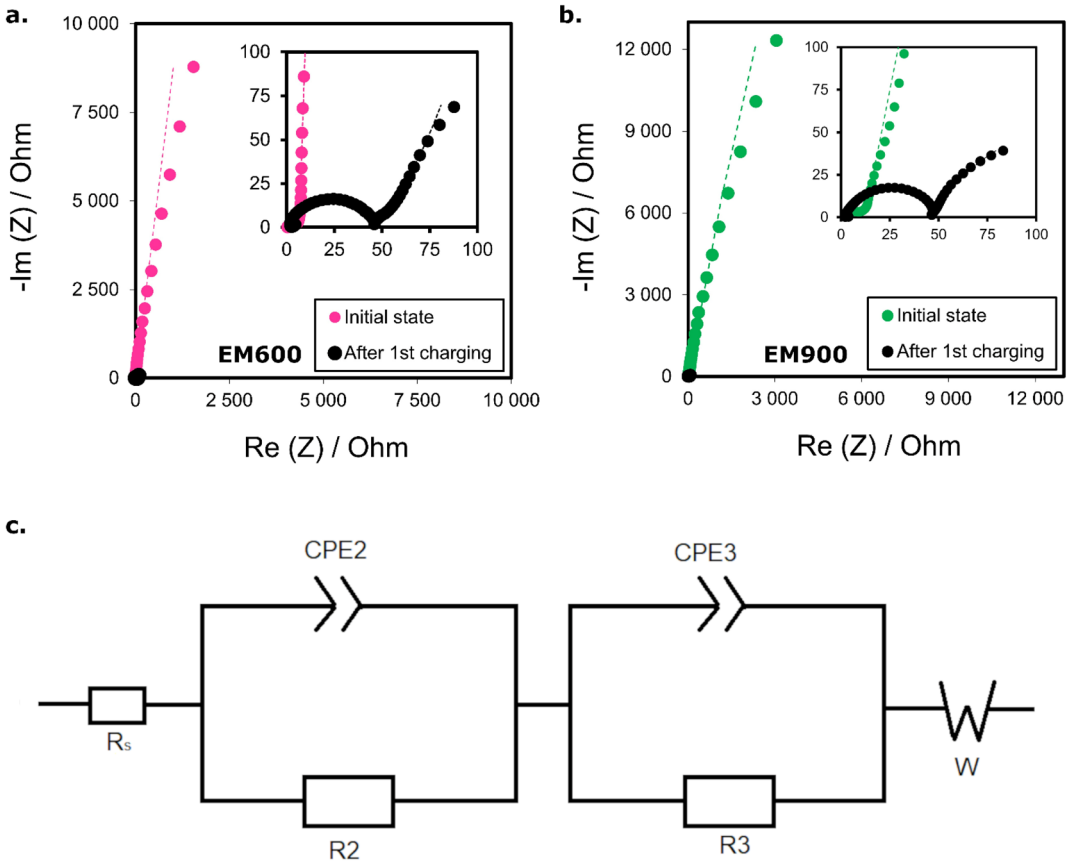

Fig. 7 Nyquist plots of EM_{600} (a) and EM_{900}-based (b) anode materials were carried out in a 3-electrode configuration. The dashed lines depict the accuracy of fitting the experimental data to an equivalent electrical circuit (c).

The Nyquist plots were fitted using the EC-Lab software to an equivalent circuit shown in Fig. 8c. Beginning from the high frequencies, the element R_s is attributed to the resistance of the electrolyte. Its values are generally small, here: close to 2 Ω for both half-cells. Next come the elements R_2 and CPE_2, which reflect together the first semi-circle. R_2 is ascribed to the resistance of the electrical double layer, which forms on the electrolyte/electrode interface. It reaches 1.41 Ω for EM_{600} and 4.32 Ω for EM_{900}. CPE_2 informs of the capacitance of this double layer. Both of them could be attributed to the SEI formation.[38] R_3 and CPE_3 could be attributed to the charge transfer resistance and capacity. R_3 values equal 39.97 Ω for EM_{600} and 37.09 Ω for EM_{900}. The SEI formation and charge transfer process explain the visible enlargement of the first semi-circles in the Nyquist plots after charging. W is a Warburg impedance which here describes a solid-state diffusion of lithium ions through the pores of the materials.

Galvanostatic charge/discharge was carried out to test the performance of both active materials. Initially, the cells were subjected to ten cycles at the current responding to the C/10, followed by ten cycles of twice faster charging and discharging at C/5. Finally, the procedure was finished with five cycles at C/10 to check the capacity retention at the end of cycling. Fig. 8 compares the charging/discharging profiles of the first and the last cycles performed at various C-rates. Fig. 8a and b present EM_{600} half-cells (first and final cycles at each rate, respectively), while Fig. 9c and d show the profiles for EM_{900} half-cell (first and final cycles at each rate, respectively). The first significant difference between the EM_{600} and EM_{900}-based cells is the amount of the consumed charge (Fig. 8a and c). At the first C/10 cycle, EM_{600} charge capacity reaches 899.7 mA h g^{-1}, but it supplies only 418.9 mA h g^{-1} upon discharge. The discrepancy is lower for EM_{900}, with 592.8 mA h g^{-1} (charge) and 311.5 mA h g^{-1} (discharge). Initially, both cells lose around half the received charge, dissipating mostly on the SEI formation. To a lesser extent, some of the lithium ions may remain captured within the pores of the carbon material. Another difference between EM_{600} and EM_{900} is the shape of the first charging/discharging profiles. The curves are steeper in the case of EM_{600}, which implies a faster potential fading of the cell. In all presented cases, the discharge capacity decreases with the increasing C-rate. It occurs because the lithium ions have less time for deintercalation from the electrode's pores. At C/5, the average discharge capacity of EM_{600} is 225.9 mA h g^{-1}, while 242.3 mA h g^{-1} for EM_{900}. Likely, the better-developed structure of highly carbonized EM_{900} opens clearer pathways for Li^+ diffusion. Moreover, the cycling test reveals better capacity retention of EM_{900}, as the difference between the first and the last cycles of each cycling step is much lower than for EM_{600}. It proves that the capacity retention of the EM_{900} is superior to

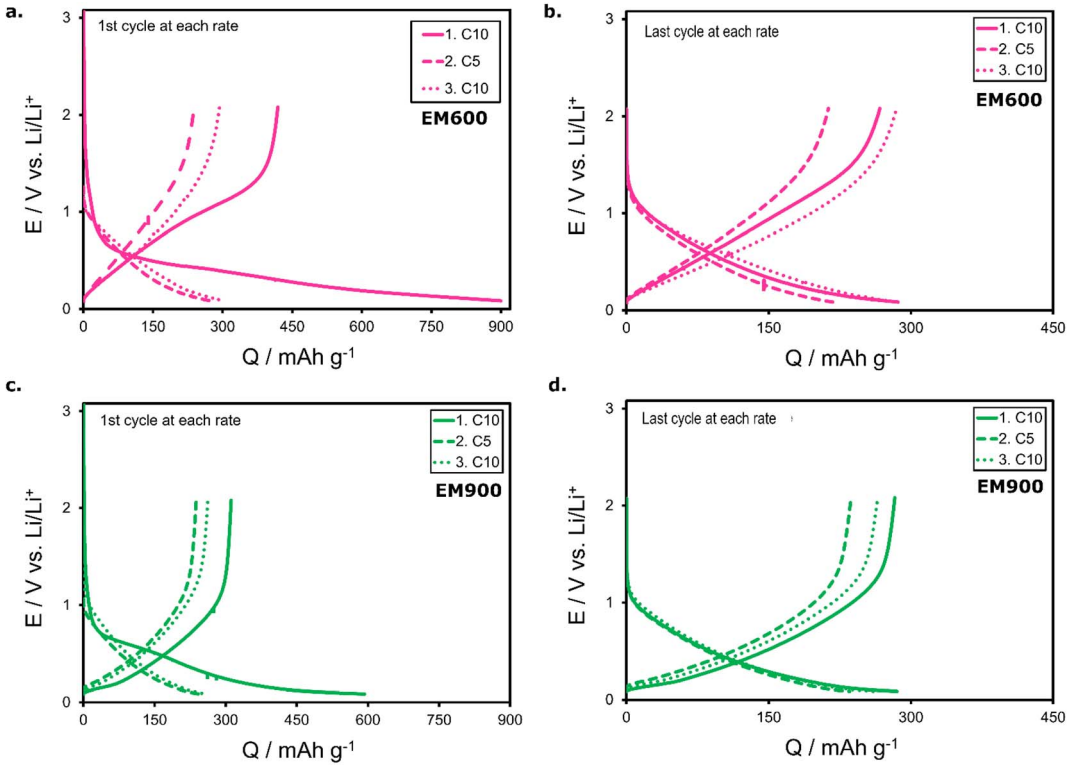

Fig. 8 Charging and discharging profiles of the first the tenth cycle of C/10 for EM_{600}-based cells (a and b – respectively) as well as for EM_{900}-based cells (c and d – respectively).

EM_{600}, reaching 84% for the former and only 68% for the latter at the end of the cycling test.

Fig. 9 illustrates the discharge capacities and cycle efficiencies of the EM_{600} and EM_{900}. The values confirm that EM_{900} operates with better stability and endures faster rates with less charge loss. EM_{600} loses around 30% of the initial discharge capacity during the first five cycles at C/10. The discharge capacity drops from 418.9 mA h g^{-1} to 267.2 mA h g^{-1} after only 10 cycles at C/10. In the case of EM_{900}, the respective values reach 311.5 mA h g^{-1} and 277.3 mA h g^{-1}. Moreover, intercalation degree x highlights the superior capacity retention of the EM_{900}, which can be observed in closer-packed curves and smaller values of the cumulative intercalation degree. EM_{600} is characterized by a high initial charging capacity, which cannot be successfully utilized during the discharge. Furthermore, the discharge capacity of EM_{600} is lower than that of EM_{900} at the rate of C/5, which could indicate a worse rate capability. After the first formation cycle, cycle efficiencies, calculated as a quotient of discharge and charge capacities, are high for both half-cells (>85%), with being superior for the more stable EM_{900} (>94%, average 98.5% from the second to last cycle). Conversely, EM_{600} consumes more current to become fully charged than during discharging.

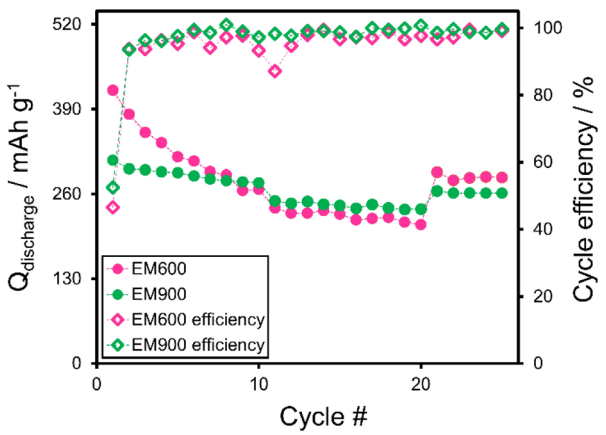

Fig. 9 Discharge capacities of the EM_{600}-based cell and EM_{900}-based cell during the cycling test.

Conclusions

In the study, we present the methods to reuse the bio-wastes such as eggshells. This sustainable and plentiful resource was converted into calcinated (outer eggshells) and carbonized (inner membranes) materials for energy storage devices. The first was used as an inert filler/scaffold in supercapacitors to substitute for activated carbon. The resulting electrodes contained less commercial activated carbon without a significant performance loss to the electrochemical capacitor. Furthermore, they were compatible with the salt-based aqueous electrolyte of Na_2SO_4, which is far more sustainable and less expensive than acid, alkaline, and organic electrolytes. The other material was directly employed for the anode in lithium-

ion batteries. Satisfying discharge capacity and relatively stable performance of EM_{600} and EM_{900} should be an incentive to pay more attention to the eggshell membrane-based anodes.

Additionally, the calcination and carbonization processes were carried out at two different temperatures: 600 and 900 °C, which affected the physicochemical and electrochemical properties of the obtained products. OS_{600}, rich in calcite and manufactured at a lower temperature, stabilized the cyclic performance of electrochemical capacitors and improved capacity retention. On the other hand, more stable performance as an anode in Li-ion batteries exhibited EM_{900}, even though both carbonized anode materials supplied similar capacities at the discharge (EM_{600}: ~280 mA h g^{-1} at C/10 and ~225 mA h g^{-1} at C/5; EM_{900}: ~270 mA h g^{-1} at C/10 and ~240 mA h g^{-1} at C/5). The higher temperature of carbonization increases the cost of the material but affects the structure of the material, making it richer in carbon with condensed aromatic rings. Hence, better operation stability of EM_{900}-based Li-ion cell. An unquestionable advantage of waste-derived electrode materials in supercapacitors and Li-ion batteries is their low price and wide availability. Such materials help reduce the amount and volume of waste that restaurants and households inevitably produce. Furthermore, the resulting electrode materials are cheaper than the commercially available activated carbons and graphites due to a cost-effective raw material and moderate thermal conditions of their processing.

Experimental

Fabrication of the active materials

Used raw chicken eggshells (EGS) were collected from local restaurants in Sydney. Initially, the ES was cleansed using tap water to remove the dust. Subsequently, they were washed with distilled water (DI) and soaked in hot DI for 30 minutes to facilitate the separation of the outer layer of eggshell (OS) from the eggshell membranes (EM).[13,17] The EM was dried at room temperature for 48 hours.[14] Fig. 2 shows the fabrication procedure and chemical composition of the eggshell membrane. Finally, dried EM and OS were processed. EM was carbonized in a pipe oven (at 600 °C and 900 °C for 3 hours, a heating rate of 5 °C min^{-1}) in a nitrogen atmosphere. Samples carbonized at 600 °C and 900 °C were labelled EM_{600} and EM_{900}, respectively. OS was calcinated in the air (at 600 °C and 900 °C for 3 h, the heating rate of 5 °C min^{-1}) and named accordingly as OS_{600} and OS_{900}.

Physicochemical characterization

Thermogravimetric analysis (TGA). Samples (approximately 15 mg each) were placed on an aluminium crucible in a Setsys 1200 (Setaram) apparatus and heated under nitrogen flow from room temperature to 1000 °C with a step of 10 °C min^{-1}. The measurements were carried out for all the obtained samples.

X-ray diffraction (XRD). The pulverized OS_{600} and OS_{900} were placed in a plastic holder. The diffractograms were recorded from 2θ of 6° to 80° using Bruker AXS D8 Advance with a step of 0.019689°.

Elemental analysis (EA). Measurements were made for EM_{600} and EM_{900} using the Vario EL III apparatus, designed to identify and quantify elements typical for organic compounds (C, S, H, N). The samples were heated to 1200 °C and burned at this exact temperature.

Fourier transform infrared spectroscopy (FTIR). Approximately 1.5 mg of a sample (EM_{600} or EM_{900}) was mixed with potassium bromide KBr and pressed to form a pellet. The spectra were recorded from 4000 to 400 cm^{-1} using an FT-IR spectrometer Bruker IFS 66v/S.

Electrode preparation and electrochemical experiments

Carbonized EM_{600} and EM_{900}, as well as calcinated OS_{600} and OS_{900}, were ground in an agate mortar to a fine powder and used as active materials in devices for energy storage. The performance of EM_{600} and EM_{900} was tested in lithium-ion batteries, while OS_{600} and OS_{900} were tested in electrochemical capacitors. The electrochemical performance of all systems was evaluated using a multichannel potentiostat/galvanostat VMP3 (BioLogic, France) with EC-Lab software.

Electrochemical capacitors

Electrode preparation. OS_{600} and OS_{900} were added to a commercial steam-activated carbon YP-80F (Kuraray, Japan, with a specific surface area of 2271 cm^2 g^{-1}) in a ratio of 1 : 9 by weight. PTFE (Sigma-Aldrich) was used as a binder while adding carbon black C65 (Imerys) enhanced the conductivity of the active material. All listed materials were mixed in a weight ratio of 85 : 10 : 5 and homogenized. Homogenized material was cut into discs (∅ 12 mm) and dried overnight at 55 °C in air. The electrolyte consisted of a 1 M aqueous solution of Na_2SO_4. Electrochemical measurements were performed in Swagelok-type T-cells in a 2- and 3-electrode configuration. When required (3-electrode configuration), the reference electrode $Hg|Hg_2SO_4$ in 0.5 M K_2SO_4 (0.68 V *vs.* NHE) was attached.

Cyclic voltammetry (CV). First, CV was performed in a 2-electrode configuration at different scan rates: 5, 10, 20, and 50 mV s^{-1}, from 0.0 V to 1.6 V. The measurement was repeated after cycling at 10 mV s^{-1}. Next, characteristics of positive and negative electrodes were scanned in a 3-electrode configuration at 5 mV s^{-1} within their respective potential ranges.

Electrochemical impedance spectroscopy (EIS). Measurements were conducted within a frequency range of 100 kHz to 1 mHz in a 2-electrode configuration.

Galvanostatic charge/discharge. The capacitors were charged and discharged with a load of 100, 200, 500, 1000, and 2000 mA g^{-1}, depending on the capability of the capacitor. Finally, supercapacitors were tested for their long cycling performance (5000 cycles, current load 1 A g^{-1}). Current loads increased when the electrodes responded well.

Lithium-ion cells

Electrode preparation. EM_{600} or EM_{900} was mixed with a binder and carbon black in the mass ratio of 85 : 10 : 5. The binder in lithium-ion batteries was PVDF (Solef® 5130, Solvay), and carbon black Super C65 (Timcal) was used as a conductive agent. A small amount of NMP (*N*-methyl-2-pyrrolidone, Sigma-Aldrich) was added to adjust the viscosity of the electrode

material in order to create a slurry that was coated on top of a copper foil (thickness 25 μm, battery-grade, Schlenk) using a doctor blade. The coated sheets were dried in air at 55 °C. Afterwards, the electrodes were cut into discs (∅ 12 mm) and dried overnight at 120 °C in a vacuum to remove moisture. The EM_{600}/Li and EM_{900}/Li half-cells were filled with commercially accepted electrolyte, 1 M $LiPF_6$ in EC : DMC 1 : 1 by volume (Sigma-Aldrich). Lithium metal (Sigma-Aldrich) was used as a counter and reference electrode.

All measurements of Li-ion half-cells were performed in a 3-electrode configuration in Swagelok-type T-cells to assess the performance of the newly obtained electrode material. The cells were assembled in a glove box (Jacomex, France) under an argon atmosphere.

Cyclic voltammetry. The measurements were carried out within the potential range of 0.05–2.0 V *vs.* Li/Li^+ at 0.01 V s^{-1} and repeated 4 times.

Electrochemical impedance spectroscopy (EIS). EIS measurements were carried out between the frequencies of 100 kHz and 10 mHz, with 10 points per decade. One measurement was performed after the cell assembly and another after a single charge.

Galvanostatic charge/discharge. The measurements were performed 10 times with the current density analogous to C/10, followed by 5 times at C/5, and finally, 5 cycles at C/10. Potential range 0.05–2.0 V *vs.* Li/Li^+.

Wettability

Wettability is the ability of a liquid to adhere to a solid substrate. Typically, the measure of wettability is the contact angle θ that forms at the liquid–solid–gas boundary. The contact angle below 90° indicates that a liquid wets the tested substrate well (the smaller θ, the better wetting). In comparison, a contact angle above 90° means poor wetting, which vanishes completely at 180°. The contact angle of the 1 M aqueous solution of Na_2SO_4 on the electrodes' surface was determined based on the sessile drop method (Fig. 10a).[39] An electrode was placed on an even glass table, and a single drop of electrolyte (V = 10 μL) was placed in the middle of the electrode (Fig. 10b and c). The wetting angle was measured using Fiji software (ImageJ). In the study, we present and discuss the average values of static contact angles obtained from two measurements for each material, using a new electrode each time.

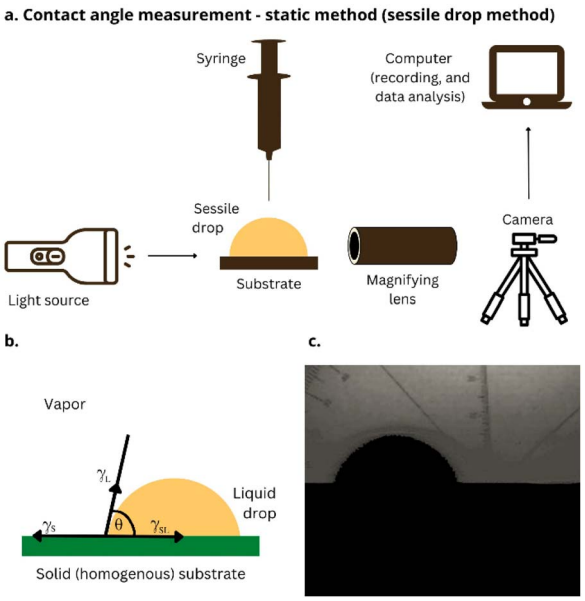

Fig. 10 Principle of the wetting angle measurements (a), contact angle at the three-phase boundary solid–liquid–atmosphere (b), an example of contact angle formed by a drop of electrolyte on an electrode made of OS_{600}+YP80F (c).

Author contributions

Agnieszka Gabryelczyk: conceptualization, methodology, investigation, writing – original draft, writing – review & editing, visualization. Sudesh Yadav: conceptualization, methodology, resources, visualization. Agnieszka Swiderska-Mocek: investigation, writing – original draft, writing – review & editing. Ali Altaee: resources, writing – review & editing. Grzegorz Lota: conceptualization, methodology, writing – review & editing, resources.

Conflicts of interest

There are no conflicts to declare.

Acknowledgements

This work was supported by the National Science Centre, Poland, grant number 2018/31/B/ST8/01619. Furthermore, the paper was created thanks to participation in program PROM of the Polish National Agency for Academic Exchange (Narodowa Agencja Wymiany Akademickiej (NAWA)) project no. POWR.03.03.00-00-PN13/18.

References

1 R. Kötz and M. Carlen, *Electrochim. Acta*, 2020, **45**, 2483.
2 D. Parra and M. K. Patel, *Appl. Energy*, 2019, **239**, 1343.
3 S. Sagadevan, A. R. Marlinda, Z. Z. Chowdhury, Y. B. A. Wahab, N. A. Hamizi, M. M. Shahid, F. Mohammad, J. Podder and M. R. Johan, in *Advances in Supercapacitor and Supercapattery. An Innovation Toward Energy Storage Devices*, Elsevier, Amsterdam, 2021, pp. 27–43.
4 B. E. Conway, *Electrochemical Supercapacitors. Scientific Fundamentals and Technological Applications*, Kluwer Academic/Plenum Publishers, New York, 1999.
5 N. H. Phan, S. Rio, C. Faur, L. Le Coq, P. Le Cloirec and T. H. Nguyen, *Carbon*, 2006, **44**, 2569.
6 M. Dizbay-Onat, U. K. Vaidya, J. A. G. Balanay and C. T. Lungu, *Adsorpt. Sci. Technol.*, 2018, **36**, 441.
7 L. Zhang, L. Tu, Y. Liang, Q. Chen, Z. Li, C. Li, Z. Wanga and W. Li, *RSC Adv.*, 2018, **8**, 42280.
8 S. Zhang, M. Zheng, Z. Lin, N. Li, Y. Liu, B. Zhao, H. Pang, J. Cao, P. He and Y. Shi, *J. Mater. Chem. A*, 2014, **2**, 15889.

9 M. Graś, Ł. Kolanowski, Z. Chen, K. Lota, K. Jurak, J. Ryl, B.-J. Ni and G. Lota, *Sustainable Energy Fuels*, 2021, **5**, 4401.
10 Z. Li, L. Zhang, B. S. Amirkhiz, X. Tan, Z. Xu, H. Wang, B. C. Olsen, C. M. B. Holt and D. Mitlin, *Adv. Energy Mater.*, 2021, **2**, 431.
11 S. Park, K. S. Choi, D. Lee, D. Kim, K. T. Li, K. H. Lee, H. Seonwoo and J. Kim, *Biosyst. Eng.*, 2016, **151**, 446.
12 M. Minakshi, H. Visbal, D. R. G. Mitchell and M. Fichtner, *Dalton Trans.*, 2018, **47**, 16828.
13 S. K. Karan, S. Maiti, S. Paria, A. Maitra, S. K. Si, J. K. Kim and B. B. Khatua, *Mater. Today Energy*, 2018, **9**, 114.
14 M. Minakshi, S. Higley, C. Baur, D. R. G. Mitchell, R. T. Jones and M. Fichtner, *RSC Adv.*, 2019, **9**, 26981.
15 L. Ma, M. Cao, C. S. Zhao, S. Huang, J. Ding, J. Chen and Y. Zhou, *Ceram. Int.*, 2021, **47**, 9118.
16 S. H. Chung and A. Manthiram, *Adv. Mater.*, 2014, **26**, 1360.
17 M. Jyothi, S. Yadav and G. Balakrishna, *J. Membr. Sci.*, 2018, **549**, 227.
18 Z. Wei, C. Xu and B. Li, *Bioresour. Technol.*, 2009, **100**, 2883.
19 P. Kamkum, N. Atiwongsangthong, R. Muanghlua and N. Vittayakorn, *Ceram. Int.*, 2015, **41**, S69.
20 X. Li, J. Liang, Z. Hou, Y. Zhu and Y. Qian, *RSC Adv.*, 2014, **4**, 50950.
21 V. H. Nguyen, D. H. Lee, S. Y. Baek and Y. H. Kim, *Mater. Lett.*, 2018, **228**, 504.
22 H. Yu, Q. Tang, J. Wu, Y. Lin, L. Fan, M. Huang, J. Lin, Y. Li and F. Yu, *J. Power Sources*, 2012, **206**, 463.
23 G. Giammaria and L. Lefferts, *J. CO2 Util.*, 2019, **33**, 341.
24 Q. Q. Lv, Y. S. Tian, J. L. Zhou, H. W. Ren and G. H. Wang, *PLoS One*, 2020, **16**, e0245124.
25 R. Mohadi, K. Anggraini, F. Riyanti and A. Lesbani, *Sri. J. Env.*, 2016, **1**, 32.
26 Y. Xie, J. Yin, J. Zheng, L. Wang, J. Wu, M. Dresselhaus and X. Zhang, *ACS Appl. Mater. Interfaces*, 2019, **11**, 32244.
27 J. Zhao, J. A. Syed, X. Wen, H. Lu and X. Meng, *J. Alloys Compd.*, 2019, **777**, 974.
28 Q. Gao, *J. Energy Chem.*, 2019, **38**, 219.
29 S. Znaniecki, K. Szwabińska, J. Wojciechowski, A. Skrzypczak and G. Lota, *ChemElectroChem*, 2021, **8**, 3685.
30 Y. Lu, X. Liu, W. Wang, J. Cheng, H. Yan, C. Tang, J.-K. Kim and Y. Luo, *Sci. Rep.*, 2015, **5**, 16584.
31 Y. Song, T. Liu, M. Li, B. Yao, T. Kou, D. Feng, F. Wang, Y. Tong, X.-X. Liu and Y. Li, *Adv. Energy Mater.*, 2018, **8**, 1801784.
32 T. Purkait, G. Singh, D. Kumar, M. Singh and R. S. Dey, *Sci. Rep.*, 2018, **8**, 640.
33 A. Turguła, M. Graś, A. Gabryelczyk, G. Lota and J. Pernak, *ChemPlusChem*, 2020, **85**, 2679.
34 W. Shang, W. Yu, X. Xiao, Y. Ma, Y. He, Z. Zhao and P. Tan, *Advanced Powder Materials*, 2023, **2**, 100075.
35 S. Bargir, S. Dunn, B. Jefferson, J. Macadam and S. Parsons, *Appl. Surf. Sci.*, 2009, **255**, 4873.
36 C. Wang, C. Piao, X. Zhai, F. N. Hickman and J. Li, *Powder Technol.*, 2010, **198**, 131.
37 D. Di Lecce, V. Gancitano and J. Hassoun, *ACS Sustainable Chem. Eng.*, 2020, **8**, 278.
38 A. Gabryelczyk, H. Smogór and A. Swiderska-Mocek, *Electrochim. Acta*, 2023, **439**, 141645.
39 J. M. Schuster, C. E. Schvezov and M. R. Rosenberg, *Procedia Mater. Sci.*, 2015, **8**, 742.